

How Physical Dynamics Shape the Properties of Ising Machines: Evaluating Oscillators vs. Bistable Latches as Ising Spins

Abir Hasan, Nikhil Shukla
University of Virginia, Charlottesville, VA, USA

Ising machines exploit the natural dynamics of physical systems to minimize the Ising Hamiltonian and thereby address computationally hard combinatorial optimization problems. This paradigm has motivated a range of physical implementations. In the electronic domain, coupled networks of oscillators and bistable latches have emerged as two prominent realizations of Ising machines and are the focus of the present work. Despite this common abstraction, we demonstrate that differences in the underlying physical dynamics of oscillators and latches lead to fundamentally different stability properties and computational behavior of the resulting dynamical systems. Specifically, we show analytically that in Bistable Latch Ising Machines (BLIMs) all discrete Ising configurations possess identical linear stability, whereas in Oscillator Ising Machines (OIMs) the Jacobian spectrum depends explicitly on the spin configuration, enabling selective destabilization of higher-energy states. Evaluating the performance of both models on MaxCut instances of varying sizes, we find that this difference in stability structure yields consistently higher-quality solutions with OIMs. These results highlight how the characteristics of the device nonlinearity directly shape the dynamical and functional properties of Ising machine implementations.

I. INTRODUCTION

The idea of exploiting the intrinsic tendency of physical systems to minimize their energy for solving computational problems finds a home in Ising machines. Such physical systems embody dynamics that aim to minimize the Ising Hamiltonian—a well-known computationally intractable problem. The Ising Hamiltonian is defined as, $H = -\sum_{i,j} J_{ij}s_i s_j$ where each spin $s \in \{+1, -1\}$, and J_{ij} denotes the coupling strength between spins i and j . Considering that many practically-relevant problems in combinatorial optimization can be expressed in terms of minimization of H [1], such Ising machines have the potential to enable accelerators for the broad class of combinatorial optimization problems (COPs).

A plethora of physical substrates spanning the quantum, optical, acoustic, mechanical and electronic domain have been evaluated for realizing Ising machines [2–4]. Nevertheless, not all spins are created equal, and the properties of the individual spins have a strong impact on the functional properties of the Ising machine. Here, we focus on the electronic implementations, specifically, using oscillators [5, 6] and bistable latches (i.e., cross-coupled inverters) [7–9] which have been commonly used to implement the underlying Ising spins.

We investigate how the choice of the spin impacts dynamical properties such as stability as well as the functional characteristics of the corresponding Ising machines, namely, Oscillator Ising Machine (OIM)

and Bistable Latch Ising Machine (BLIM). We note that manifestations of BLIM include BRIM (Bistable, Resistively Coupled Ising Machines) [10, 11]. We assume resistive coupling in all our analysis.

II. DYNAMICS OF BLIM

We first focus on the dynamical properties of the BLIM and subsequently compare them to those of the Kuramoto oscillator-based Ising machine, which has been extensively studied in prior work [12–14]. Starting with a single bistable latch, the normalized internal state $\nu_i(t)$ evolves according to [7],

$$\dot{\nu}_i = \frac{\tanh(k \tanh(k\nu_i)) - \nu_i}{\tau}, \quad (1)$$

where ν_i is the dimensionless latch state variable (with saturated values $\nu_i \approx \pm 1$ corresponding to the two logical states), $k > 0$ is a dimensionless gain parameter controlling the sharpness of the nonlinearity, and τ is the intrinsic latch time constant. In an RC realization, τ is proportional to an RC (R : Resistance C : Capacitance) product (e.g., $\tau = RC$), setting the relaxation rate of an isolated latch.

When coupled with other latches, the resulting dynamics can be expressed as,

$$\begin{aligned} \dot{\nu}_i &= \frac{\tanh(k \tanh(k\nu_i)) - \nu_i}{\tau} - \left[\sum_{\substack{j=1 \\ j \neq i}}^N \frac{A_{ij}^+(\nu_i - \nu_j)}{\tau_c} + \sum_{\substack{j=1 \\ j \neq i}}^N \frac{A_{ij}^-(\nu_i - (-\tanh(k\nu_j)))}{\tau_c} \right], \\ &= \frac{\tanh(k \tanh(k\nu_i)) - \nu_i}{\tau} - \frac{1}{\tau_c} \left[\sum_{\substack{j=1 \\ j \neq i}}^N (A_{ij}^+ + A_{ij}^-) \nu_i - \sum_{\substack{j=1 \\ j \neq i}}^N A_{ij}^+ \nu_j + \sum_{\substack{j=1 \\ j \neq i}}^N A_{ij}^- \tanh(k\nu_j) \right], \end{aligned} \quad (2)$$

where τ_c is the coupling time constant associated with the interconnection circuitry. The positive and negative entries of the symmetric adjacency (coupling) matrix $A \in \mathbb{R}^{N \times N}$ are separated as,

$$A_{ij}^+ = \max(A_{ij}, 0), \quad A_{ij}^- = \max(-A_{ij}, 0), \quad (3)$$

so that $A_{ij}^+, A_{ij}^- \geq 0$, and

$$A = A^+ - A^-. \quad (4)$$

Under this decomposition, A^+ encodes ferromagnetic (at-

tractive) interactions and A^- encodes the *magnitude* of the antiferromagnetic (repulsive) interactions.

Eq (2) reveals an asymmetry in the dynamics for ferromagnetic and antiferromagnetic coupling in the BLIM with an additional nonlinear transformation on ν_j , $\tanh(k\nu_j)$, appearing in the interaction. This feature was also noted in [9].

Examining from an energetics standpoint, the dynamics in Eq. (2) can be considered to perform gradient descent on a energy function that can be expressed as,

$$E(\nu) = \sum_{i=1}^N U(\nu_i) - \frac{1}{2\tau_c} \left[\sum_{ij} (A_{ij}^+) \nu_i \nu_j - \sum_{ij} (A_{ij}^-) \nu_i \tanh(k\nu_j) - \sum_i (d_i^+ + d_i^-) \nu_i^2 \right]. \quad (5)$$

where $U'(\nu) = -g(\nu)$, i.e., $U(\nu) = -\int^\nu g(\xi) d\xi$. Furthermore, $d_i^\pm = \sum_j A_{ij}^\pm$, where d_i^\pm denote the absolute weighted degrees associated with the positive and negative edges, respectively.

At the fixed points $\nu \in \{-1, +1\}$, the energy function in Eq. (5) can be approximated to represent Ising spins, since $\tanh(k\nu_j) \approx \nu_j$ as the dynamics settle to the saturated states $\nu \in \{-1, +1\}$ (see Appendix A). A sufficiently large gain k ensures that the state of the nodes approaches $\nu \rightarrow \pm 1$. In this regime, the energy function reduces to

$$E(\nu) \equiv H = C - \frac{K}{2} \left[\sum_{ij} A_{ij} s_i s_j \right], \quad (6)$$

where,

$$C \approx \sum_{i=1}^N U(\nu_i) + \frac{1}{2\tau_c} \sum_i (d_i^+ + d_i^-)$$

is a constant offset and $K = \frac{1}{\tau_c}$.

Figure 1(a) shows the dynamics of a BLIM simulated for a randomly generated graph with 15 nodes and 50 negatively coupled edges. The nodes are initialized to $\nu = 0$. As expected from the discussion above, ν diverges

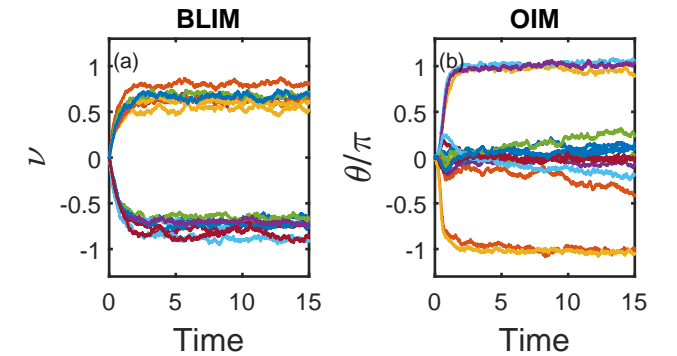


FIG. 1: Temporal evolution of the state of the node in (a) BLIM, and (b) OIM, simulated on a randomly generated graph with 15 nodes and 50 edges. Simulation parameters: BLIM: $\tau = 1$, $\tau_c = 12$ $k = 10$; $K_n = 0.05$; OIM: $K_{osc} = 1$; $K_s = 1.5$; $K_n = 0.05$

towards $\nu = -1$ or $\nu = +1$. For comparison, the dynamics of OIM (Eq. (17)) which uses oscillators under second harmonic injection have been included as Fig. 1(b).

III. LINEAR STABILITY OF BLIM

We now analyze the linear stability of the BLIM dynamics and compare it with that of the OIM. In the saturated regime $\nu \rightarrow \pm 1$, corresponding to the Ising fixed points, the nonlinearity can be approximated as $\tanh(k\nu_j) \approx \nu_j$, and Eq. (2) reduces to,

$$\begin{aligned} \dot{\nu}_i &= \frac{\tanh(k \tanh(k\nu_i)) - \nu_i}{\tau} - \left[\sum_{\substack{j=1 \\ j \neq i}}^N \frac{A_{ij}^+(\nu_i - \nu_j)}{\tau_c} + \sum_{\substack{j=1 \\ j \neq i}}^N \frac{A_{ij}^-(\nu_i - (-\nu_j))}{\tau_c} \right], \\ &= \frac{\tanh(k \tanh(k\nu_i)) - \nu_i}{\tau} - \frac{1}{\tau_c} \left[\sum_{\substack{j=1 \\ j \neq i}}^N (A_{ij}^+ + A_{ij}^-) \nu_i - \sum_{\substack{j=1 \\ j \neq i}}^N (A_{ij}^+ - A_{ij}^-) \nu_j \right]. \end{aligned} \quad (7)$$

Defining the elementwise nonlinearity $g(\nu_i) \equiv [\tanh(k \tanh(k\nu_i)) - \nu_i]/\tau$ and the absolute weighted degree

$$d_i \equiv \sum_{\substack{j=1 \\ j \neq i}}^N (A_{ij}^+ + A_{ij}^-), \quad D \equiv \text{diag}(d_1, \dots, d_N), \quad (8)$$

Eq. (7) can be written compactly as,

$$\dot{\boldsymbol{\nu}} = \mathbf{G}(\boldsymbol{\nu}) - \frac{1}{\tau_c} \boldsymbol{\Gamma} \boldsymbol{\nu}, \quad \boldsymbol{\Gamma} \equiv D - (A^+ - A^-), \quad (9)$$

where $\mathbf{G}(\boldsymbol{\nu})$ applies $g(\cdot)$ elementwise.

For the purely ferromagnetic case, $A_{ij}^- = 0 \Rightarrow \boldsymbol{\Gamma} = D - (A_{ij}^+ - A_{ij}^-) = D - A$. Consequently, $\boldsymbol{\Gamma}$ then represents the *Laplacian* \mathbf{L} of the graph. In contrast, for the purely anti-ferromagnetic case, $A_{ij}^+ = 0 \Rightarrow \boldsymbol{\Gamma} = D + A_{ij}^- = D + |A|$, which effectively represents the *signless Laplacian*, \mathbf{Q} , of the graph.

Equation (7) reveals an important structural feature of the latch dynamics: each node contains a degree-dependent self-term that effectively introduces a local bias in the dynamics. Although, as seen from the energy function in Eq. (5), this term does not alter the mapping to the Ising Hamiltonian at the binary states, it modifies the local field experienced by each node during the transient evolution.

Equation (7) can be also be expressed as,

$$\dot{\nu}_i = g(\nu_i) - \frac{1}{\tau_c} \left[\underbrace{(d_i^+ + d_i^-)}_{\substack{\text{absolute weighted} \\ \text{degree-dependent} \\ \text{offset}}} \nu_i - \sum_j (A_{ij}^+ - A_{ij}^-) \nu_j \right], \quad (10)$$

which shows that the dynamics of each node i is influenced by a self-bias term whose influence is asymmetrically controlled by $(d_i^+ + d_i^-)$ in the general case. Comparing the above dynamics to the OIM, the degree-dependent self-bias term can be viewed as being structurally analogous to the onsite SHI term $K_s \sin(2\theta_i)$ in the OIM dynamics (Eq. (17)), if the K_s strength is made proportional to the absolute weighted degree of the individual nodes. Nevertheless, the precise functional forms are different.

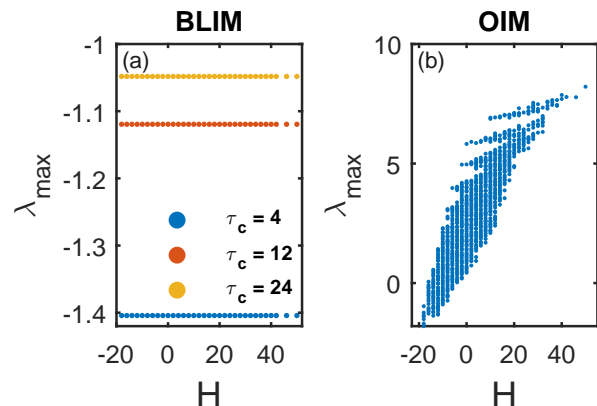


FIG. 2: Comparison of maximal Jacobian eigenvalues (λ_{\max}) across all Ising configurations for (a) the BLIM and (b) the OIM. The same graph as in Fig. 1 is considered. In the BLIM, λ_{\max} is identical for all configurations at fixed τ_c , indicating configuration-independent linear stability. In the OIM, λ_{\max} depends explicitly on the spin configuration, reflecting configuration-dependent stability. $k = 2$ (BLIM) and $K_s = 1.5$ (OIM).

Linearizing the dynamics in Eq. (9) about an equilibrium

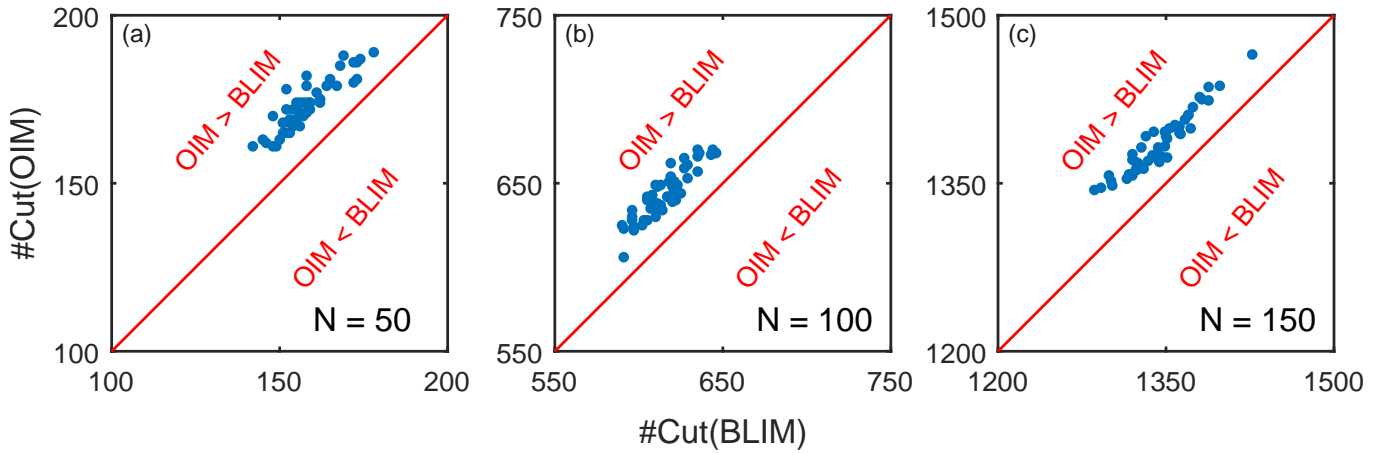


FIG. 3: Comparison of MaxCut values obtained using OIM and BLIM dynamics across 150 random graphs. (a) $N = 50$, (b) $N = 100$, and (c) $N = 150$ nodes (50 instances per size). Each point represents one graph; the red diagonal (identity line) denotes equal performance. In all tested instances, the OIM achieved a cut value greater than that of the BLIM.

point ν^* yields the Jacobian

$$\begin{aligned} J(\nu^*) &= \text{diag}(g'(\nu_i^*)) - \frac{1}{\tau_c} \Gamma \\ &= \text{diag}(g'(\nu_i^*)) - \frac{1}{\tau_c} (D + |A|) \end{aligned} \quad (11)$$

since we focus on the anti-ferromagnetic case, which corresponds directly to the MaxCut COP formulation evaluated in the subsequent sections. Here, D refers to the absolute weighted degree.

The off-diagonal entries of the Jacobian can be expressed as,

$$J_{ij} = -\frac{1}{\tau_c} |A_{ij}|, \quad i \neq j, \quad (12)$$

which are *independent* of the operating point. All state dependence enters exclusively through the diagonal terms,

$$J_{ii} = g'(\nu_i^*) - \frac{d_i}{\tau_c}. \quad (13)$$

where, d_i refers to the absolute unweighted degree of the i^{th} node.

We now restrict attention to Ising configurations, $\nu_i^* = s_i \in \{-1, +1\}$. Here, we assume that k is large enough to approximate s as fixed points. Owing to the symmetry of the latch nonlinearity, $g'(1) = g'(-1)$, implying

$$\text{diag}(g'(s_i)) = g'(1) I, \quad (14)$$

where I refers to an identity matrix. Consequently, at every Ising configuration,

$$J = g'(1) I - \frac{1}{\tau_c} (D + |A|), \quad (15)$$

which is independent of the specific spin assignment \mathbf{s} . The maximal real eigenvalue therefore satisfies

$$\lambda_{\max} = g'(1) - \frac{1}{\tau_c} \lambda_{\min}(D + |A|), \quad (16)$$

and is identical for all Ising configurations of a given graph. Linear stability of all discrete states, $\nu \in \{-1, +1\}$, is thus uniform.

Comparison with OIMs

In contrast to BLIM, OIMs which are governed by phase dynamics of the form:

$$\dot{\theta}_i = -K_{\text{osc}} \sum_j A_{ij} \sin(\theta_i - \theta_j) - K_s \sin(2\theta_i), \quad (17)$$

exhibit a fundamentally different linearization structure. Linearizing Eq. (17) about an Ising configuration $\theta_i^* \in \{0, \pi\}$ yields off-diagonal Jacobian entries

$$J_{ij} = K_{\text{osc}} A_{ij} \cos(\theta_i^* - \theta_j^*), \quad i \neq j. \quad (18)$$

Since $\cos(\theta_i^* - \theta_j^*) = s_i s_j$, the Jacobian explicitly depends on the spin configuration. Consequently, the spectrum of the Jacobian varies across Ising states and Ising energy. A detailed analysis of OIM linear stability has been reported in prior work [13]. Furthermore, Allibhoy *et al.* [15] have shown that the conditional expectation of the eigenvalues of the Jacobian decreases with reducing Ising energy making them more likely to be stabilized.

This distinction between the linear stability properties of the BLIM and the OIM is illustrated in Fig. 2 using the same graph considered in Fig. 1. For the BLIM (Fig. 2(a)), the maximal eigenvalue λ_{\max} remains constant across all the Ising configurations, and therefore is independent of the Ising energy, for a fixed τ_c .

Consequently, this produces *horizontal bands* when plotted against Ising energy H . Here, λ_{\max} denotes the largest eigenvalue of the Jacobian; $\lambda_{\max} < 0$ indicates asymptotic stability of the corresponding configuration, whereas $\lambda_{\max} > 0$ indicates instability. In contrast, the OIM (Fig. 2(b)) exhibits a broad distribution of λ_{\max} values that depend on the Ising energy, reflecting configuration-dependent linear stability.

To assess the practical implications of the stability structure derived above, we evaluate the performance of the BLIM and the OIM on the MaxCut problem. We consider Erdős–Rényi random graphs of different sizes ($N = 50$, $N = 100$, and $N = 150$ nodes) each generated with an edge probability of 0.2. 50 instances are considered for each size. Furthermore, each graph is simulated five times using both, the BLIM and the OIM dynamics, and the best cut obtained across the five runs from each dynamic is reported and compared.

For the BLIM, the parameters are set to $k_{\max} = 10$, $\tau = 1$, and $\tau_c = 4$. For the OIM, we use $K_{\text{osc}} = 1$ and $K_{s_{\max}} = 1.5$. During the simulation, the gain parameter k for the BLIM and the second-harmonic injection strength K_s for the OIM are periodically varied between 0 and their respective maximum values (k_{\max} and $K_{s_{\max}}$) using a square-wave schedule. This schedule facilitates the periodic stabilization and destabilization of the Ising fixed points which subsequently improves the resulting solution. The simulation parameters are as follows: (a) Total simulation period $T_f = 15$; (b) Time step $\Delta t = 10^{-4}$; (c) Time period of square wave schedule for k and K_s , $T_p = 6$; (d) During each trial, the solution is sampled at $T = \{1.5, 7, 13\}$ when $k = k_{\max}$ and $K_s = K_{s_{\max}}$. The systems are initialized at $\nu_i = 0$ (BLIM) and $\phi_i = 0$ (OIM), respectively. The OIM is initialized at $\phi_i = 0$ because this initialization yields better cuts compared to the commonly used random initialization, which tends to exhibit higher levels of spin freezing [16].

Figure 3 compares the cut values obtained by both dynamics. Each point corresponds to one graph; the red line is the identity line ($y = x$) indicating equal performance. Points above the diagonal indicate that the OIM yielded a higher cut. Across all graph sizes, the OIM dynamics provided higher cuts in comparison to the BLIM in every instance. This empirical trend aligns with the linear stability analysis: whereas the BLIM exhibits configuration-independent Jacobian spectra at Ising states, the OIM possesses configuration-dependent stability, effectively destabilizing higher-Ising energy (lower cut) configurations and biasing the dynamics toward improved cuts.

IV. CONCLUSION

In this work, we elucidate fundamental differences in the dynamical properties of BLIMs and OIMs arising from differences in the underlying non-linearity

of the spin. Oscillator-based implementations exhibit configuration-dependent linear stability, whereas bistable latch-based Ising machine designs result in identical stability at all discrete Ising configurations. The differing dynamical properties subsequently impact the computational properties of the two systems. In OIMs, the ability to selectively destabilize higher-energy configurations may confer a performance advantage relative to BLIMs, although bistable latch implementations may offer practical advantages in terms of simplicity and ease of realization.

ACKNOWLEDGEMENT

This material is based upon work supported by ARO award W911NF-24-1-0228.

DATA AVAILABILITY

The data that support the findings of this study are available from the corresponding author upon request.

CODE AVAILABILITY

The codes associated with this manuscript are available from the corresponding author upon request.

Appendix A: Reduction of the Cross-Coupled Latch Dynamics to a Single Differential State

Here, we demonstrate that under mild symmetry conditions the bistable latch dynamics collapse onto an invariant manifold, permitting the approximation $\nu'_i \approx -\nu_i$ after the initial transient dynamics.

Consider a symmetric cross-coupled inverter pair described by

$$\dot{\nu}_i = \frac{g(\nu'_i) - \nu_i}{\tau}, \quad \dot{\nu}'_i = \frac{g(\nu_i) - \nu'_i}{\tau}, \quad (\text{A1})$$

where ν_i and ν'_i denote the normalized node voltages on the two complementary sides of the latch, τ is the intrinsic latch time constant, and $g(\cdot)$ represents the static inverter transfer characteristic. In the present work,

$$g(\nu) = \tanh(k \tanh(k\nu)), \quad (\text{A2})$$

which is an odd, saturating nonlinearity.

To analyze the symmetry of the dynamics, we define differential and common-mode variables

$$\mu_i \equiv \frac{\nu_i - \nu'_i}{2}, \quad \varepsilon_i \equiv \frac{\nu_i + \nu'_i}{2}. \quad (\text{A3})$$

Expressing the node voltages in terms of these variables,

$$\nu_i = \varepsilon_i + \mu_i, \quad \nu'_i = \varepsilon_i - \mu_i. \quad (\text{A4})$$

Substituting these expressions into Eq. (A1) yields

$$\begin{aligned} \dot{\mu}_i &= \frac{1}{2\tau} \left[g(\varepsilon_i - \mu_i) - g(\varepsilon_i + \mu_i) - 2\mu_i \right], \\ \dot{\varepsilon}_i &= \frac{1}{2\tau} \left[g(\varepsilon_i - \mu_i) + g(\varepsilon_i + \mu_i) - 2\varepsilon_i \right]. \end{aligned} \quad (\text{A5})$$

Since $g(\cdot)$ is odd,

$$g(-\nu) = -g(\nu). \quad (\text{A6})$$

Evaluating Eq. (A5) on the subspace $\varepsilon_i = 0$ gives

$$\dot{\mu}_i = \frac{g(\mu_i) - \mu_i}{\tau}, \quad (\text{A7})$$

$$\dot{\varepsilon}_i = -\frac{\varepsilon_i}{\tau}. \quad (\text{A8})$$

Equation (A8) shows that the common-mode variable ε_i decays exponentially with rate $1/\tau$. Consequently, the subspace $\varepsilon_i = 0$ is an invariant and linearly stable manifold of the dynamics. Any initial common-mode perturbation relaxes toward zero on the intrinsic latch time scale.

On this invariant manifold the dynamics reduce exactly to

$$\dot{\mu}_i = \frac{g(\mu_i) - \mu_i}{\tau}. \quad (\text{A9})$$

Using $\nu_i = \varepsilon_i + \mu_i$ and $\nu'_i = \varepsilon_i - \mu_i$, and noting that $\varepsilon_i \rightarrow 0$, we obtain

$$\nu'_i \approx -\nu_i. \quad (\text{A10})$$

Starting from the symmetric initialization $\nu_i = 0$, this approximation becomes increasingly accurate as the system evolves and the latch states approach the saturated values $\nu_i \rightarrow \pm 1$.

Appendix B: Impact of coupling strength on BLIM dynamics

In this section, we investigate the impact of coupling strength and latch gain on the dynamics of the BLIM.

Simulation framework: Figure 4 shows simulation results for a BLIM implementing a 15-node graph with 50 edges (same as the graph considered in Fig. 1). Simulations were performed in MATLAB[®] using the built-in stochastic differential equation (SDE) solver based on the Euler–Maruyama method. The simulated SDE with additive white Gaussian noise (AWGN) is

$$d\boldsymbol{\nu} = \left(\mathbf{G}(\boldsymbol{\nu}) - \frac{1}{\tau_c} \Gamma \boldsymbol{\nu} \right) dt + K_n I dW_t, \quad (\text{B1})$$

where $K_n = 0.05$, I is the identity matrix, and dW_t denotes a Wiener process. The spin state is extracted as $s = \text{sign}(\boldsymbol{\nu})$. All simulations shown in Fig. 4 are initialized at $\boldsymbol{\nu} = 0$. The framework considered here is the same as that employed to generate the results in Fig. 1(a).

Figures 4(a)–(d) show representative time evolution of the latch states for increasing τ_c , which inversely controls the effective coupling strength i.e., larger τ_c corresponds to weaker coupling. The corresponding equilibrium energy distributions over 100 independent trials are shown in Fig. 4(e)–(h).

As τ_c increases, we observe that the probability of reaching the ground state decreases and higher-energy configurations become more prevalent. For the example graph considered here, the dynamics converge to the ground state ($H = -18$) in 35 out of 100 trials for $\tau_c = 4$, whereas no ground-state solutions are observed for $\tau_c = 24$ or $\tau_c = 100$.

Figures 4(i)–(l) show representative trajectories for increasing latch gain k (with τ_c fixed), and Figs. 4(m)–(p) show the corresponding equilibrium energy distributions over 100 independent trials. A similar trend is observed: increasing k reduces the probability of attaining the ground state and increases the likelihood of convergence to higher-energy configurations.

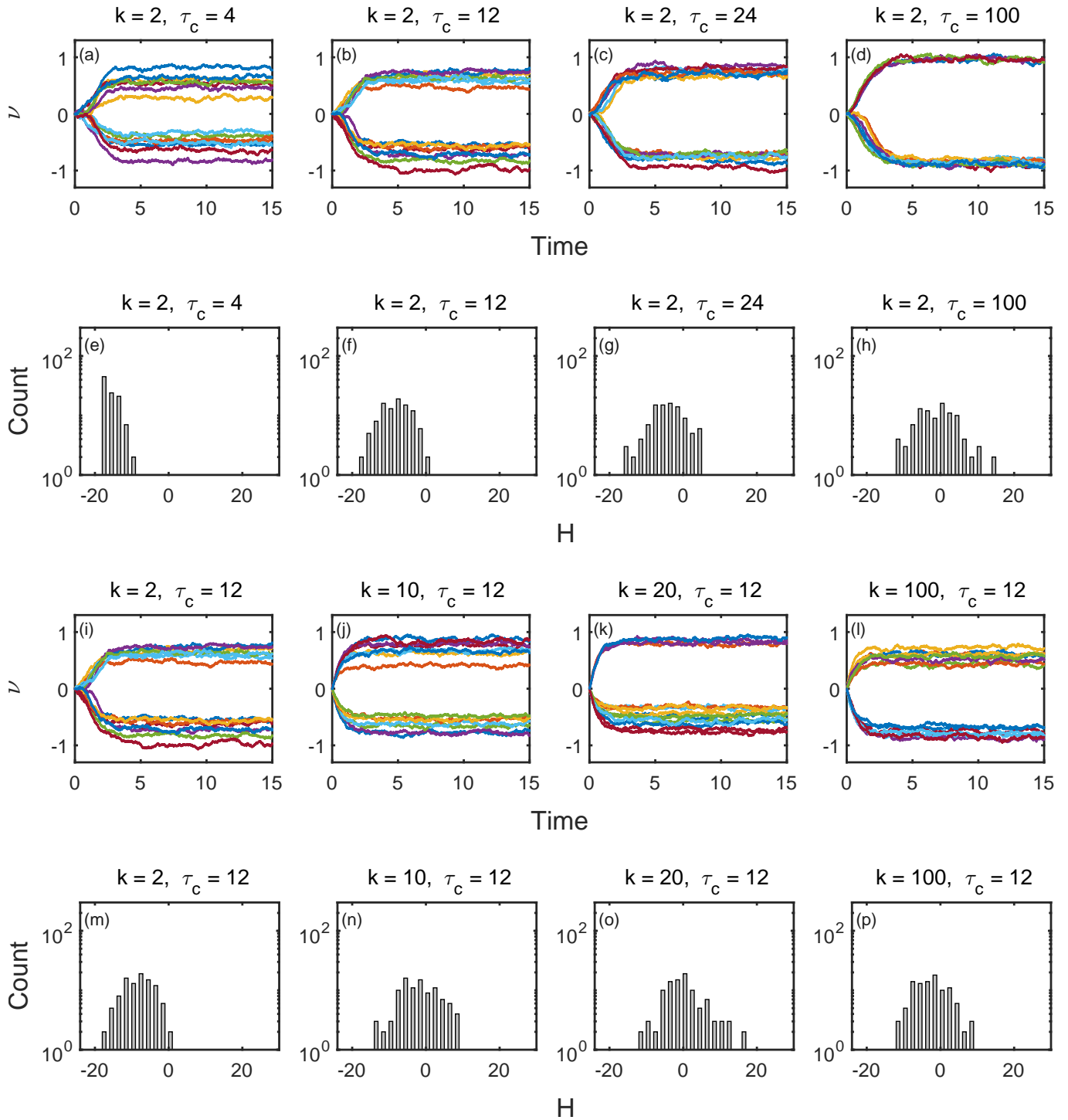


FIG. 4: Influence of τ_c and k on BLIM dynamics. (a)–(d) Representative time evolution of node states for increasing τ_c (with fixed $k = 2$). (e)–(h) Histograms of the Ising energy of configurations obtained at equilibrium over 100 independent trials for the corresponding τ_c values. (i)–(l) Time evolution of node states for increasing gain k (with fixed $\tau_c = 12$). (m)–(p) Energy histograms obtained over 100 independent trials for the corresponding k values.

REFERENCES

- [1] A. Lucas, Ising formulations of many NP problems, *Frontiers in Physics*, vol. 2, 2014.
- [2] N. Mohseni, P. L. McMahon, and T. Byrnes, Ising machines as hardware solvers of combinatorial optimization problems, *Nature Reviews Physics*, vol. 4, no. 6, pp. 363–379, 2022.
- [3] A. Todri-Sanial, C. Delacour, M. Abernot, and F. Sabo, Computing with oscillators from theoretical underpinnings to applications and demonstrators, *npj Unconventional Computing*, vol. 1, no. 1, p. 14, 2024.
- [4] A. Litvinenko, R. Khymyn, R. Ovcharov, and J. Åkerman, A 50-spin surface acoustic wave Ising machine, *Communications Physics*, vol. 8, no. 1, p. 58, 2025.
- [5] A. Mallick, M. K. Bashar, D. S. Truesdell, B. H. Calhoun, and N. Shukla, Overcoming the accuracy vs. performance trade-off in oscillator Ising machines, in *IEEE International Electron Devices Meeting (IEDM)*, 2021.
- [6] M. K. Bashar, A. Mallick, D. S. Truesdell, B. H. Calhoun, S. Joshi, and N. Shukla, Experimental demonstration of a reconfigurable coupled oscillator platform to solve the Max-Cut problem, *IEEE Journal on Exploratory Solid-State Computational Devices and Circuits*, vol. 6, no. 2, pp. 116–121, 2020.
- [7] J. Roychowdhury, Bistable latch Ising machines, in *Unconventional Computation and Natural Computation*, Springer, 2021.
- [8] A. Mallick et al., CMOS-compatible Ising machines built using bistable latches coupled through ferroelectric transistor arrays, *Scientific Reports*, vol. 13, no. 1, p. 1515, 2023.
- [9] J.-H. Hung and J. Roychowdhury, A study on advanced Ising machine designs: BLIM, King’s graph mapping, and OIM chips, Tech. Rep., EECS Department, University of California, Berkeley, 2024.
- [10] Y. Zhang et al., A CMOS compatible bistable resistively-coupled Ising machine (BRIM), in *IEEE International Symposium on Circuits and Systems*, 2022.
- [11] E. Elmitwalli, Z. Ignjatovic, and S. Kose, Utilizing multi-body interactions in a CMOS-based Ising machine for LDPC decoding, *IEEE Transactions on Circuits and Systems I*, vol. 71, no. 1, pp. 40–50, 2024.
- [12] M. K. Bashar, Z. Lin, and N. Shukla, Stability of oscillator Ising machines: Not all solutions are created equal, *Journal of Applied Physics*, vol. 134, no. 14, 2023.
- [13] Y. Cheng, M. K. Bashar, N. Shukla, and Z. Lin, A control theoretic analysis of oscillator Ising machines, *Chaos*, vol. 34, no. 7, 2024.
- [14] T. Wang and J. Roychowdhury, Oscillator-based Ising machines for solving combinatorial optimisation problems, *arXiv:1903.07163*, 2019.
- [15] A. Allibhoy, A. N. Montanari, F. Pasqualetti, and A. E. Motter, Global optimization through heterogeneous oscillator Ising machines, in *IEEE Conference on Decision and Control*, 2025.
- [16] M. Farasat, E. M. H. E. B. Ekanayake, and N. Shukla, Spin freezing in oscillator Ising machines: When second-harmonic injection impedes computation, *Physical Review Applied*, 2026.